IEEE Open Journal of the
Industrial Electronics Society

Received 27 February 2023; revised 14 April 2023 and 15 May 2023; accepted 6 June 2023. Date of publication 12 June 2023; date of current version 21 June 2023. The review of this paper was arranged by Associate Editor Xi Chen.

Digital Object Identifier 10.1109/OJIES.2023.3285010

Enhanced Frequency Control for Power-Synchronized PLL-Less Grid-Following Inverters

NABIL MOHAMMED [1] (Member, IEEE), MOHAMMAD HASAN RAVANJI [2] (Member, IEEE), WEIHUA ZHOU [1] (Member, IEEE), AND BEHROOZ BAHRANI [1] (Senior Member, IEEE)

[1]Department of Electrical and Computer Systems Engineering, Monash University, Clayton, VIC 3800, Australia
[2]Department of Electrical Engineering, Sharif University of Technology, Tehran P932+FM4, Iran

CORRESPONDING AUTHOR: NABIL MOHAMMED (e-mail: nabil.mohammed@ieee.org)

This work was supported in part by the Monash Grid Innovation Hub and in part by the Australian Renewable Energy Agency (ARENA) through the Advancing Renewable Program under Grant 2020/ARP007.

ABSTRACT This article presents an enhanced power-synchronized grid-following inverter (ePSGFLI) for reliable and stable integration of renewable energy resources into the grid. By eliminating the use of a phase-locked loop (PLL) in the control loop, the ePSGFLI resolves instability issues commonly associated with conventional PLL-based grid-following inverters (GFLIs). Furthermore, in contrast to existing PLL-less strategies like linear parameter-varying control of power-synchronized GFLI (LPV-PSGFLI), which suffer from steady-state errors and instability during grid frequency deviations, the proposed ePSGFLI ensures stable performance without steady-state errors, regardless of the strength of the grid. To achieve robust and accurate tracking of grid frequency, even under significant deviations, while effectively decoupling the active and reactive power loops, the ePSGFLI employs a loop-shaping design procedure for real-time auto-tuning of the multivariable second-order 2-by-2 outer power controller. The effectiveness of the proposed ePSGFLI is validated via simulations in MATLAB/Simulink and experimental testing under both strong and weak grid connections. The results demonstrate its superior performance compared to existing PLL-based and PLL-less control strategies in terms of stable operation and accurate tracking of power and grid frequency.

INDEX TERMS Adaptive control, phase-locked loop (PLL), PLL-less inverters, power-synchronized control, stability, weak grid.

I. INTRODUCTION

Grid-connected inverters play a critical role in the integration of renewable energy resources into existing power systems [1], [2]. These inverters can be categorized into two main types based on their synchronization approach—grid-following inverters (GFLIs) and grid-forming inverters (GFMIs) [3], [4], [5], [6]. GFLIs rely on phase-locked loop (PLL) control, utilizing the measurement of the point of common coupling (PCC) voltage to synchronize with the grid [7], [8], while GFMIs estimate the required grid frequency for synchronization through active power-frequency droop control [9]. GFLIs demonstrate reliable performance in strong grids, which are characterized by high short-circuit ratios (SCR) [10], but their performance deteriorates in weak grids due to the negative resistance introduced by the PLL at low frequencies [11], [12], [13].

The existing control strategies for resolving PLL-related instability issues are broadly categorized into two groups: 1) enhancing the control of PLL-based GFLIs; and 2) proposing PLL-less control strategies. In [14], a comprehensive explanation is provided regarding the dynamics of advanced PLLs within the *dq*-frame impedance model employed for three-phase GFLIs. Currently, wind and solar photovoltaic systems frequently employ the synchronous reference frame (SRF)-PLL for synchronization with the grid frequency [15], [16]. Numerous techniques are proposed in the literature to improve the performance of PLL-based inverters. For example, in [17], a symmetric structure for the PLL is proposed to eliminate

the frequency coupling between the d- and q-axes, thus, enhancing stability. The proposed double-PLL-based improved control scheme in [18] extends the stability range even when the PLL bandwidth is high. Additional improvements to PLL-based inverters include PLL controller retuning [11], [15], a new PLL structure [17], [18], and introducing an artificial bus between the real PCC and the grid as a reference point of the PLL [19]. In [20], a feedback linearization controller is proposed to expand the PLL domain of attraction, thus, enhancing the GFLI performance in weak and strong grids.

Numerous PLL-less techniques have been proposed for GFLIs operating in weak grids that eliminate the need for the PLL. Direct power control (DPC), introduced in [21] and [22], is a noteworthy example of such a technique, as it does not necessitate a PLL for either grid synchronization or an inner current control loop. However, the inability to restrict inverter output current and maintain a consistent switching frequency is one of the significant drawbacks of this approach. In [23] and [24], a model predictive control-DPC (MPC-DPC) strategy is developed to achieve a constant switching frequency. Nevertheless, the primary issue with the MPC-DPC technique is the excessive computational burden. To ensure rapid output power convergence, an enhanced grid voltage modulated direct power control (GVM-DPC) is proposed in [25]. However, this approach necessitates an ideal grid voltage to design the GVM-DPC method, which is impractical since the grid voltage can be distorted by various background noises, such as harmonics, interharmonics, and subharmonics [26], [27], [28].

There has been a growing interest in the development of PLL-less control strategies for GFLIs in recent years. One promising approach is the voltage-modulated direct power control (VMDPC) proposed for three-phase GFLI in [29]. This method eliminates the need for the PLL and does not require an ideal grid voltage. However, the use of a band-pass filter (BPF) in the VMDPC control loop to extract the fundamental grid voltage can adversely affect the system dynamics. Furthermore, the VMDPC necessitates the inverter to generate a specific amount of reactive power to deliver the rated active power to a weak grid. While the VMDPC represents an improvement over the PLL-based method, its benefits are only marginally better [30]

A power-synchronized PLL-less grid-following inverter (PSGFLI) is proposed in [31], which regulates the terminal power. Hence, the inverter can operate reliably in strong, weak, and even ultraweak grids as no PCC voltage sensing/regulation is needed. In this method, the vector current control is deployed in the inner loop, while the outer power loop is used to extract the grid frequency and generate the current references. The dynamic performance of the controller is tuned by choosing a desired open-loop transfer function. Despite the effectiveness of this method, the optimization-based tuning of the outer power loop in the design stage is complex and dependent on the operating point. Hence, the optimal performance depends on the specific operating point that the system is tuned to.

In [32], linear parameter-varying control of power-synchronized grid-following inverter (LPV-PSGFLI) to overcome the control design limitations in [31]. The parameters of the outer power controller loop are auto-tuned in real-time based on the desired operating points. Furthermore, the LPV-PSGFLI preserves the benefits of the PSGFLI as it can effectively operate in both stiff and weak grid conditions. However, the major limitation of the LPV-PSGFLI is the type of controller used in the outer power loop. The current references are generated using two PI controllers, but there are no integral terms in the power control channels responsible for generating the frequency. Therefore, any deviation in the grid frequency from the nominal value not only causes steady-state errors in the inverter output active and reactive powers, but can also drive the inverter to instability.

This paper proposes an enhanced power-synchronized PLL-less grid-following inverter (ePSGFLI) to address the challenges faced by existing control approaches such as the PSGFLI and LPV-PSGFLI, while preserving their advantages. Similar to the PSGFLI and LPV-PSGFLI, the proposed ePSGFLI method does not require a PCC voltage or a PLL to regulate the power exchange with the grid, making it robust in both strong and weak grid connections. The inner current control of the ePSGFLI is similar to the GFLI, while the outer power loop is used to generate the frequency and the d-component of the current reference (the q-component is set to zero). The main contributions of this article are as follows.

1) A detailed and accurate model of the power flow equations when the injected current is aligned with the q-component is derived.
2) A loop-shaping design procedure of a second-order 2-by-2 controller for the outer power loop based on the derived model is proposed. This enables the ePSGFLI to cope with large grid frequency deviations without causing any steady-state errors in the inverter output power or being driven to unstable operations.
3) The parameters of the proposed outer power controller are tuned adaptively in real-time based on the operating point of the inverter. As a result, the bandwidth of the power control loop remains fixed at the desired value regardless of the power reference commands and the grid conditions, such as strong and weak grids.

The rest of this article is organized as follows. Section II discusses the modeling and limitations of the power-synchronized control strategy for PLL-less GFLIs. Section III describes the proposed control approach. Sections IV and V present the simulation and experimental results to verify the effectiveness of the proposed control scheme. Finally, Section VI concludes this article.

II. MODELING OF POWER-SYNCHRONIZED CONTROL STRATEGY FOR GFLIs

This section briefly presents the control structure and derivation of the small-signal model of the PSGFLI since it is utilized in Section III to design the proposed control strategy.

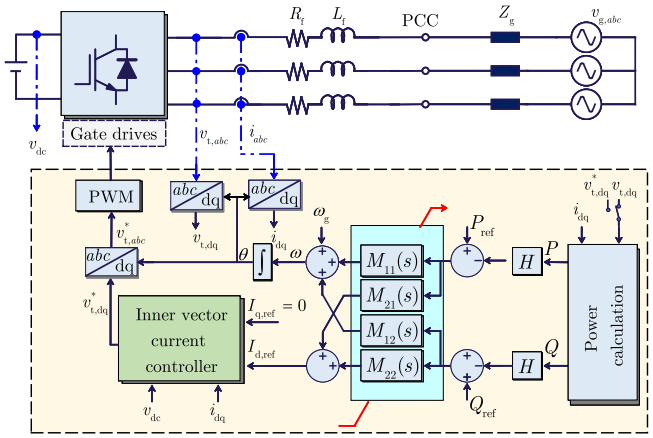

FIGURE 1. Proposed enhanced power-synchronized PLL-less grid-following inverter.

A. CONTROL STRUCTURE OF PSGFLI

The block diagram of the PSGFLI is depicted in Fig. 1. The presented PLL-less control approach [31], [32] is capable of operating seamlessly across a wide range of grid strengths, without being prone to instability. The control technique regulates the active and reactive power output of the inverter at the inverter terminal, rather than at the PCC. Thus, it utilizes the terminal voltage ($v_{t,abc}$) and output current (i_{abc}) to achieve this objective. As the power/voltage is regulated at the inverter terminal rather than at the PCC, the voltage utilized in the inverter controller can either be the measured ($v_{t,abc}$) or the PWM reference voltage ($v^*_{t,abc}$). The latter approach has the advantage of being free of any switching harmonics. Moreover, it obviates the requirement for voltage measurement at the terminal and reduces the expenses related to a voltage sensor.

B. SMALL-SIGNAL MODELING OF PSGFLI

The power-synchronized control strategy assumes that the rotating reference frame is aligned with the inverter output current, resulting in $i_q = 0$ A [31]. Thus, the inverter output current and voltage can be written in the dq reference frame as

$$i_{dq} = I_d + j0, \tag{1}$$

$$v_{t,dq} = V_t \cos\theta + jV_t \sin\theta \tag{2}$$

where θ represents the angle between the inverter terminal voltage and the inverter output current, I_d denotes the d-component of the inverter output current, and V_t denotes the magnitude of the inverter output phase-to-neutral voltage. Furthermore, the inverter output active and reactive powers can be expressed as

$$P + jQ = \frac{3}{2}(V_t I_d \cos\theta + jV_t I_d \sin\theta). \tag{3}$$

Equation (3) reveals that the active and reactive power are directly proportional to the d-component and q-component of the inverter terminal voltage, respectively.

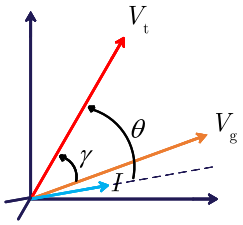

FIGURE 2. Phasor diagram of the system.

Assuming small perturbations around θ and $I_{d,ref}$, i.e., $\theta = \theta_0 + \Delta\theta$ and $I_d = I_{d,0} + \Delta I_d$, the small-signal model is obtained by linearizing (3) around the operating point $(\theta_0, I_{d,0})$ of the system. The resulting small-signal model is

$$\begin{bmatrix}\Delta P\\ \Delta Q\end{bmatrix} = \begin{bmatrix}\frac{3}{2}I_{d,0}\cos\theta_0\\ \frac{3}{2}I_{d,0}\sin\theta_0\end{bmatrix}\Delta V_t + \begin{bmatrix}\frac{-3}{2}V_t I_{d,0}\sin\theta_0 & \frac{3}{2}V_t\cos\theta_0\\ \frac{3}{2}V_t I_{d,0}\cos\theta_0 & \frac{3}{2}V_t\sin\theta_0.\end{bmatrix}\begin{bmatrix}\Delta\theta\\ \Delta I_d\end{bmatrix}. \tag{4}$$

In (4), it can be noticed that the small perturbations around the operating point result in variations in the d and q components of the terminal voltage ($v_{t,d}$, $v_{t,q}$). To better understand the system, it is helpful to consider the voltage and current phasors. Fig. 2 shows the phasors for the block diagram of the inverter presented in Fig. 1, where V_g is the magnitude of the grid voltage $v_{g,abc}$ and I is the magnitude of the inverter output current i_{abc}. The dq-components of the terminal voltage can be expressed as

$$\begin{aligned} V_{t,d} &= V_g\cos(\theta-\gamma) + (R_t + sL_t)I_d\\ V_{t,q} &= V_g\sin(\theta-\gamma) + L_t\omega_0 I_d \end{aligned} \tag{5}$$

in which γ represents the angle between the grid voltage and the terminal voltage. To further analyze the system, (5) can be rewritten based on the phasor diagram between voltage and current as

$$(V_{t,d} - (R_t + sL_t)I_d)^2 + (V_{t,q} - L_t I_d)^2 = V_g^2 \tag{6}$$

$$\begin{aligned}&(\Delta V_{t,d} - (R_t + sL_t)\Delta I_d)(V_{t,d,0} - (R_t + sL_t)I_{d,0})\\ &+(\Delta V_{t,q} - L_t\omega_0\Delta I_d)(V_{t,q,0} - L_t\omega_0 I_{d,0}) = 0.\end{aligned} \tag{7}$$

Since $V_{t,d} = V_t\cos\delta$ and $V_{t,q} = V_t\sin\delta$, one can write

$$\begin{aligned}\Delta V_{t,d} &= \Delta V_t\cos\theta_0 - V_{t,0}\sin\theta_0\Delta\theta\\ \Delta V_{t,q} &= \Delta V_t\sin\theta_0 + V_{t,0}\cos\theta_0\Delta\theta.\end{aligned} \tag{8}$$

By replacing for $\Delta V_{t,d}$ and $\Delta V_{t,q}$ from (8) in (6) and (7), one can write

$$\begin{aligned}&(\Delta V_t\cos\theta_0)(V_{t,d,0} - (R_t + sL_t)I_{d,0})\\ &-(V_{t,0}\sin\theta_0\Delta\theta + (R_t + sL_t)\Delta I_d)(V_{t,d,0} - (R_t + sL_t)I_{d,0})\\ &+(\Delta V_t\sin\theta_0)(V_{t,q,0} - L_t\omega_0 I_{d,0})\\ &+(V_{t,0}\cos\theta_0\Delta\theta - L_t\omega_0\Delta I_d)(V_{t,q,0} - L_t\omega_0 I_{d,0}) = 0.\end{aligned} \tag{9}$$

Additionally, (9) can be rearranged as

$$\begin{aligned}\Delta V_{\mathrm{t}}&(\cos\theta_0(V_{\mathrm{t,d,0}}-(R_{\mathrm{t}}+sL_{\mathrm{t}})I_{\mathrm{t,d,0}}+\sin\theta_0(V_{\mathrm{t,q,0}}-L_{\mathrm{t}}\omega_0 I_{\mathrm{d,0}}))\\&=\Delta\theta(V_{\mathrm{t,0}}\sin\theta_0(V_{\mathrm{t,d,0}}-(R_{\mathrm{t}}+sL_{\mathrm{t}})I_{\mathrm{d,0}})\\&\quad-V_{\mathrm{t,0}}\cos\theta_0(V_{\mathrm{t,q,0}}-L_{\mathrm{t}}\omega_0 I_{\mathrm{d,0}}))\\&\quad+\Delta I_{\mathrm{d}}((R_{\mathrm{t}}+sL_{\mathrm{t}})(V_{\mathrm{t,d,0}}-(R_{\mathrm{t}}+sL_{\mathrm{t}})I_{\mathrm{d,0}})\\&\quad+L_{\mathrm{t}}\omega_0(V_{\mathrm{t,q,0}}-L_{\mathrm{t}}\omega_0 I_{\mathrm{d,0}})).\end{aligned}\tag{10}$$

Assuming the current controller is fast and $X_{\mathrm{t}}=L_{\mathrm{t}}\omega_0$, (10) can be written as presented in the following:

Assuming sinusoidal operation for the system when $\Delta\theta$ and ΔI_{d} are injected, the expression in (11) shown at the bottom of this page, simplifies to

$$\begin{aligned}\Delta V_{\mathrm{t}}=&\frac{V_{\mathrm{t,0}}I_{\mathrm{d,0}}(L_{\mathrm{t}}\omega_0\cos\theta_0-R_{\mathrm{t}}\sin\theta_0)}{V_{\mathrm{t,0}}-[R_{\mathrm{t}}\cos\theta_0+L_{\mathrm{t}}\omega_0\sin\theta_0]I_{d0}}\Delta\theta\\&+\frac{V_{\mathrm{t,0}}(R_{\mathrm{t}}\cos\theta_0+L_{\mathrm{t}}\omega_0\sin\theta_0)-I_{\mathrm{d,0}}(R_{\mathrm{t}}^2+(L_{\mathrm{t}}\omega_0)^2)}{V_{\mathrm{t,0}}-[R_{\mathrm{t}}\cos\theta_0+L_{\mathrm{t}}\omega_0\sin\theta_0]I_{\mathrm{d,0}}}\Delta I_{\mathrm{d}}.\end{aligned}\tag{12}$$

By substituting for ΔV_{t} from (12) into (4), the plant model is obtained as follows:

$$\begin{bmatrix}\Delta P\\ \Delta Q\end{bmatrix}=\begin{bmatrix}\frac{-3}{2}V_{\mathrm{t,0}}I_{\mathrm{d,0}}\sin\theta_0+\frac{3}{2}I_{\mathrm{d,0}}\cos\theta_0 a_1 & \frac{3}{2}V_{\mathrm{t,0}}\cos\theta_0+\frac{3}{2}I_{\mathrm{d,0}}\cos\theta_0 a_2\\ \frac{3}{2}V_{\mathrm{t,0}}I_{\mathrm{d,0}}\cos\theta_0+\frac{3}{2}I_{\mathrm{d,0}}\sin\theta_0 a_1 & \frac{3}{2}V_{\mathrm{t,0}}\sin\theta_0+\frac{3}{2}I_{\mathrm{d,0}}\sin\theta_0 a_2\end{bmatrix}\begin{bmatrix}\Delta\theta\\ \Delta I_{\mathrm{d}}\end{bmatrix}\tag{13}$$

where a_1 and a_2 are given by

$$a_1=\frac{V_{\mathrm{t,0}}I_{\mathrm{t,d,0}}(L_{\mathrm{t}}\omega_0\cos\theta_0-R_{\mathrm{t}}\sin\theta_0)}{V_{\mathrm{t,0}}-I_{\mathrm{t,d,0}}(R_{\mathrm{t}}\cos\theta_0+L_{\mathrm{t}}\omega_0\sin\theta_0)}\tag{14}$$

$$a_2=\frac{V_{\mathrm{t,0}}(R_{\mathrm{t}}\cos\theta_0+L_{\mathrm{t}}\omega_0\sin\theta_0)-I_{\mathrm{t,d,0}}(R_{\mathrm{t}}^2+(L_{\mathrm{t}}\omega_0)^2)}{V_{\mathrm{t,0}}-I_{\mathrm{t,d,0}}(R_{\mathrm{t}}\cos\theta_0+L_{\mathrm{t}}\omega_0\sin\theta_0)}\tag{15}$$

where R_{t} and L_{t} are the equivalent resistance and inductance of the inverter output filter (R_{f} and L_{f}) and the grid impedance (R_{g} and L_{g}). These parameters can be expressed as

$$\begin{aligned}R_{\mathrm{t}}&=R_{\mathrm{f}}+R_{\mathrm{g}}\\L_{\mathrm{t}}&=L_{\mathrm{f}}+L_{\mathrm{g}}.\end{aligned}\tag{16}$$

Considering $\omega=-\frac{d\theta}{dt}$, H is the low-pass filter (LPF) used to filter the calculated active and reactive power, and the transfer function of the current controller, the plant model in (13) can be rewritten as

$$\begin{bmatrix}\Delta P\\ \Delta Q\end{bmatrix}=\frac{3}{2}\begin{bmatrix}\frac{V_{\mathrm{t,0}}I_{\mathrm{d,0}}\sin\theta_0-I_{\mathrm{d,0}}\cos\theta_0 a_1}{s}H & \frac{V_{\mathrm{t,0}}\cos\theta_0+3I_{\mathrm{d,0}}\cos\theta_0 a_2}{1+\tau s}H\\ \frac{-V_{\mathrm{t,0}}I_{\mathrm{d,0}}\cos\theta_0-3I_{\mathrm{d,0}}\sin\theta_0 a_1}{s}H & \frac{V_{\mathrm{t,0}}\sin\theta_0+3I_{\mathrm{d,0}}\sin\theta_0 a_2}{1+\tau s}H\end{bmatrix}\begin{bmatrix}\Delta\omega\\ \Delta I_{\mathrm{d,ref}}\end{bmatrix}\tag{17}$$

where θ_0 is the initial angle between the inverter voltage and current at the operating point. $I_{\mathrm{d,0}}$ is the inverter output current d-component. Furthermore, ω is the angular frequency of the grid estimated by the inverter. Equation (17) can be written in a compact form as

$$\begin{bmatrix}\Delta P\\ \Delta Q\end{bmatrix}=G\times\begin{bmatrix}\Delta\omega\\ \Delta I_{\mathrm{d,ref}}\end{bmatrix}.\tag{18}$$

Considering τ is the time constant of the current controller, the closed-loop transfer function of the current controller is written as

$$G_{\mathrm{cc}}=\frac{1}{\tau s+1}.\tag{19}$$

The adopted second-order LPF has the following transfer function:

$$H=\frac{\omega_{\mathrm{f}}^2}{s^2+2\zeta\omega_{\mathrm{f}}s+{\omega_{\mathrm{f}}}^2}\tag{20}$$

where ζ and ω_{f} are the damping ratio and natural frequency of the filter, respectively.

The block diagram of the PSGFLI is illustrated in Fig. 1. It can be observed that the outer power loop, which is responsible for tracking the inverter output power, consists of a 2-by-2 multiple-input multiple-output (MIMO) control system. In [31], it is demonstrated that the transfer functions $M_{11}(s)$ through $M_{22}(s)$ are proportional-integral (PI) compensators. However, the optimization-based design methodology for tuning these four PI compensators is not straightforward. Furthermore, the PSGFLI inverter exhibits instability in rectification mode due to the negative gain margin of the system.

In [32], the LPV-PSGFLI is proposed for the auto-tuning of the four transfer functions of the power controller. However, this proposed control strategy in deploys only two PI compensators and two pure gains in the LPV-PSGFLI, making it susceptible to steady-state errors in the inverter output power and instability for any deviation in the grid frequency from the nominal value. To overcome the aforementioned limitations of the existing PSGFLI and LPV-PSGFLI strategies, this article proposes an enhanced second-order control strategy referred to as ePSGFLI. The details of this strategy are elaborated in the following section.

III. PROPOSED ePSGFLI

A. CONTROL DESIGN USING LOOP SHAPING

The proposed ePSGFLI shares a similar structure with PSGFLI shown in Fig. 1, with differences only found in the

$$\Delta V_{\mathrm{t}}=\frac{V_{\mathrm{t,0}}I_{\mathrm{d,0}}(L_{\mathrm{t}}\omega_0\cos\theta_0-(R_{\mathrm{t}}+sL_{\mathrm{t}})\sin\theta_0)}{V_{\mathrm{t,0}}-[(R_{\mathrm{t}}+sL_{\mathrm{t}})\cos\theta_0+L_{\mathrm{t}}\omega_0\sin\theta_0]I_{\mathrm{d,0}}}\Delta\theta+\frac{V_{\mathrm{t,0}}((R_{\mathrm{t}}+sL_{\mathrm{t}})\cos\theta_0+L_{\mathrm{t}}\omega_0\sin\theta_0)-I_{\mathrm{d,0}}((R_{\mathrm{t}}+sL_{\mathrm{t}})^2+(L_{\mathrm{t}}\omega_0)^2)}{V_{\mathrm{t,0}}-[(R_{\mathrm{t}}+sL_{\mathrm{t}})\cos\theta_0+L_{\mathrm{t}}\omega_0\sin\theta_0]I_{\mathrm{d,0}}}\Delta I_{\mathrm{d}}.\tag{11}$$

equations for $M_{11}(s)$ to $M_{22}(s)$. These equations are designed using the loop-shaping procedure based on the desired open-loop transfer function matrix of the system (L_D). Accordingly, Fig. 1 also depicts the block diagram of the proposed ePS-GFLI. For the ePSGFLI, to ensure decoupling and achieve the desired dynamic performance under frequency deviations, the desired open-loop transfer function matrix of the system is selected as follows:

$$L_D = \begin{bmatrix} L_{D11} & 0 \\ 0 & L_{D22} \end{bmatrix} = \begin{bmatrix} \frac{\omega_c(s+\alpha)}{s^2} & 0 \\ 0 & \frac{\omega_c(s+\alpha)}{s^2} \end{bmatrix}. \tag{21}$$

It is noteworthy that the diagonal elements of L_D represent second-order transfer functions, where ω_c can be chosen to achieve the desired closed-loop bandwidth of the system. Moreover, $(s+\alpha)$ represents the zero of the desired open-loop transfer function matrix, which is necessary for ensuring system stability. By utilizing the loop-shaping-based approach, the parameters of the proposed second-order 2-by-2 controller can be calculated as

$$M = G^{-1} \times L_D. \tag{22}$$

Referring to the plant model in (17) and (18) and neglecting the LPF H, the parameters of the proposed multivariable 2-by-2 controller for the outer power control loop of the ePSGFLI can be derived as demonstrated in the following:

$$M(s) = \begin{bmatrix} \underbrace{K_{11}\frac{\omega_c(s+\alpha)}{s}}_{M_{11}(s)} & \underbrace{K_{12}\frac{\omega_c(s+\alpha)}{s}}_{M_{12}(s)} \\ \underbrace{K_{21}\frac{\omega_c(s+\alpha)(\tau s+1)}{s^2}}_{M_{21}(s)} & \underbrace{K_{22}\frac{\omega_c(s+\alpha)(\tau s+1)}{s^2}}_{M_{22}(s)} \end{bmatrix} \tag{23}$$

where

$$\begin{cases} K_{11} = 2\sin\theta_0/(3I_{\mathrm{d},0}V_{\mathrm{t},0}) \\ K_{12} = -2\cos\theta_0/(3I_{\mathrm{d},0}V_{\mathrm{t},0}) \\ K_{21} = 2\left(\cos\theta_0 + \frac{a_1}{V_{\mathrm{t},0}}\sin\theta_0\right) \Big/ \left(3V_{\mathrm{t},0}\left(1+\frac{I_{\mathrm{d},0}}{V_{\mathrm{t},0}}a_2\right)\right) \\ K_{22} = 2\left(\sin\theta_0 - \frac{a_1}{V_{\mathrm{t},0}}\cos\theta_0\right) \Big/ \left(3V_{\mathrm{t},0}\left(1+\frac{I_{\mathrm{d},0}}{V_{\mathrm{t},0}}a_2\right)\right). \end{cases} \tag{24}$$

It is worth noting that each term of the proposed 2-by-2 controller comprises two components: a fixed part and an adaptive part. Specifically, the fixed parts in $M_{11}(s)$ and $M_{12}(s)$ employ two PI controllers, while two second-order transfer functions are employed for the fixed parts in $M_{11}(s)$ to $M_{12}(s)$. The adaptive terms in the proposed controller in $M_{11}(s)$ and $M_{12}(s)$ are denoted by K_{11} to K_{22}. These adaptive terms are calculated in real-time by (24) to preserve a fixed controller bandwidth regardless of the inverter operating point.

In the proposed adaptive tuning method, presented in (24), the required parameters ($V_{\mathrm{t},0}$, $I_{\mathrm{d},0}$, θ_0, a_1, and a_1) to calculate K_{11} to K_{22} at any operating point (P_{ref}, Q_{ref}) are straightforward to obtain. First, $V_{\mathrm{t},0}$ is calculated from the inverter terminal voltage components or references to the PWM, as $V_{\mathrm{t},0} = \sqrt{V_{\mathrm{d},0}^2 + V_{\mathrm{q},0}^2}$. Second, $I_{\mathrm{d},0}$ is calculated from P_{ref} and Q_{ref} as $I_{\mathrm{d},0} = P_{\mathrm{ref}}/(1.5V_{\mathrm{d},0})$. Third, θ_0 is calculated as $\theta_0 = Q_{\mathrm{ref}}/Q_{\mathrm{d},0}$. The parameters a_1 and a_2 are calculated from (14) and (15), respectively.

In comparison to the PSGFLI and LPV-PSGFLI proposed in [31] and [32], respectively, the proposed ePSGFLI in (23) provides several significant advantages. One key advantage is its ability to handle grid frequency deviations effectively while ensuring zero steady-state errors in the inverter output power, which guarantees stable operation even under large frequency deviations. Another advantage is that it maintains the desired bandwidth of the system, as the proposed 2-by-2 controllers ($M_{11}(s)$ to $M_{22}(s)$) are adaptively tuned for any operating point (P_{ref}, Q_{ref}). In contrast, the PSGFLI method relies on optimization-based tuning and cannot maintain a fixed system bandwidth for all operating points. Additionally, the LPV-PSGFLI uses pure gains for $M_{11}(s)$ and $M_{12}(s)$, which results in steady-state errors when the grid frequency deviates from the nominal value and may lead to instability.

B. STABILITY ANALYSIS

To analyze the stability of the proposed control under different grid conditions, different approaches could be used. In this work, the small-signal impedance-based stability analysis using both the Bode plot and the generalized Nyquist criterion (GNC) is chosen owing to its common usage in power electronics research. Initially, the output impedances of the proposed PLL-less ePSGFLI are obtained in the dq reference frame. Then, the Bode plot and the GNC are used to calculate the margins and predict the stability under different grid conditions.

Moreover, the obtained results are compared with the conventional PLL-based GFLI, referred to as GFLI, which is equipped with an inner current controller and generates its current references from an outer open-loop power control. Both control systems are evaluated under identical grid conditions for each test. The three tested grid conditions correspond to a strong grid with SCR = 10, a weak grid with SCR = 2, and a very weak grid with SCR = 1.2, denoted by $Z_{\mathrm{g}1}$, $Z_{\mathrm{g}2}$, and $Z_{\mathrm{g}3}$, respectively. It is worth mentioning that the output impedances of both the conventional GFLI and ePSGFLI are obtained when the power references are set to $P_{\mathrm{ref}} = 4$ MW and $Q_{\mathrm{ref}} = 0$ Var.

Figs. 3 and 4 illustrate the stability comparison of the GFLI and ePSGFLI strategies, respectively. On the one hand, Fig. 3(a) and (c) presents the Bode plot of the grid impedances and output impedance of the GFLI in the d-axis ($Z_{\mathrm{odd-GFLI}}$) and q-axis ($Z_{\mathrm{oqq-GFLI}}$), respectively. It can be observed that while the inverter will be stable in the d-axis, it will not be stable in the q-axis when connected to a very weak grid, as the phase margin at the intersection frequency of 80 Hz is 201°>180°. On the other hand, Fig. 4(a) and (c) shows the Bode plot of the grid impedances and output impedance of the ePSGFLI in the d-axis ($Z_{\mathrm{odd-ePSGFLI}}$) and q-axis ($Z_{\mathrm{oqq-ePSGFLI}}$), respectively. It is predicted that the

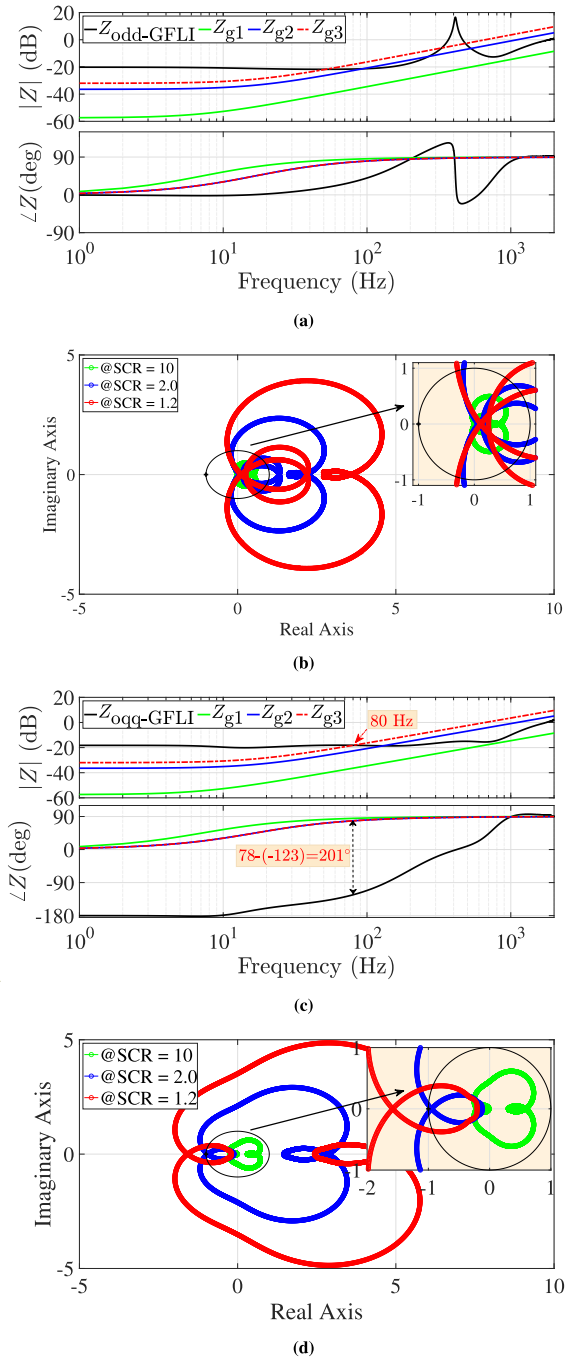

FIGURE 3. Impedance-based stability analysis of the conventional PLL-based GFLI in three grid conditions (SCR = 10, 2, 1.2). (a) and (c) Bode plots of the grid impedances and the inverter output impedances in the *d*-axis and *q*-axis, respectively. (b) and (d) Nyquist plots in the *d*-axis and *q*-axis, respectively.

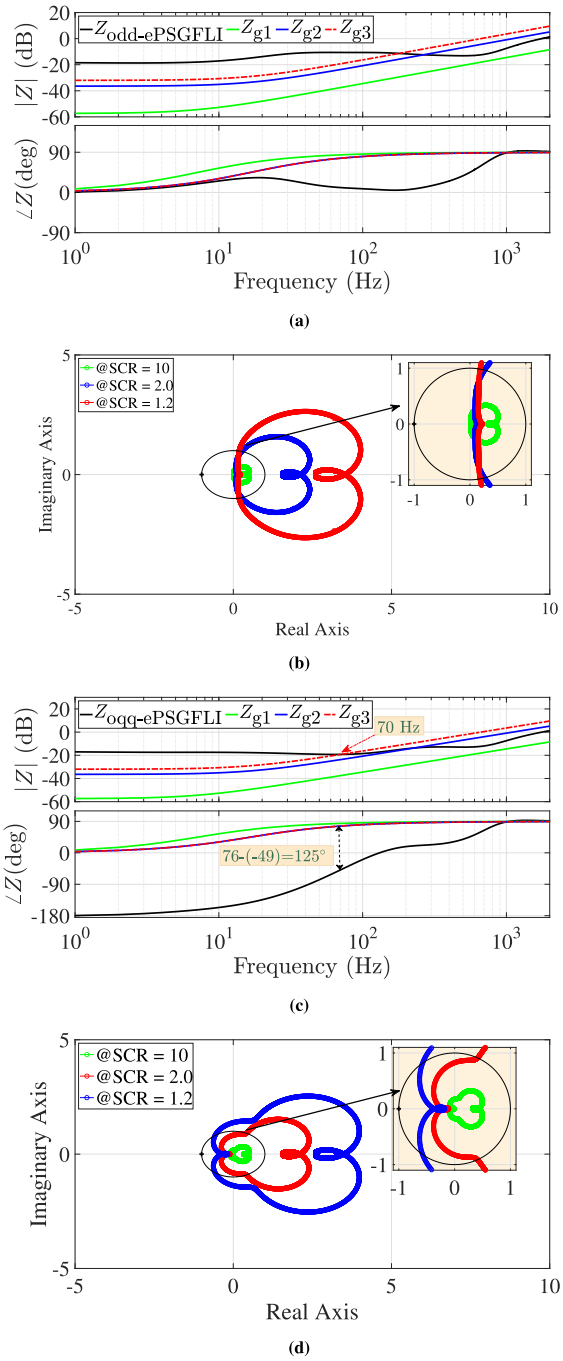

FIGURE 4. Impedance-based stability analysis of the proposed PLL-less ePSGFLI in three grid conditions (SCR = 10, 2, 1.2). (a) and (c) Bode plots of the grid impedances and the inverter output impedances in the *d*-axis and *q*-axis, respectively. (b) and (d) Nyquist plots in the *d*-axis and *q*-axis, respectively.

ePSGFLI will be stable in both the *d*-axis and *q*-axis owing to its larger phase margins, thereby enhancing its resilience to grid impedance variations. For instance, the phase margin at the intersection frequency of 70 Hz when SCR = 1.2 is $125° \ll 180°$.

Figs. 3(b) and 4(b) show the Nyquist plots in the *d*-axis for the GFLI and the ePSGFLI, respectively. It is observed that both controllers exhibit stability in the *d*-axis for all tested grid connections. However, as shown in Fig. 3(d), the GFLI is only stable in the *q*-axis when connected to the strong grid (shown

TABLE 1. Parameters Used for the Simulation Study

Parameter	Symbol	Value	Unit
Grid voltage (RMS, L-L)	v_g	690	V
Grid nominal frequency	f_g	50	Hz
Strong grid with SCR = 10	R_g, L_g	1.35, 30	mΩ, μH
Weak grid with SCR = 2	R_g, L_g	15, 144	mΩ, μH
Inverter rated active power	P_n	4	MW
Inverter rated reactive power	Q_n	3	MVar
DC bus voltage	v_{dc}	3	kV
Filter inductance	L_f	95	μH
Filter resistance	R_f	10	mΩ
Inverter PWM carrier frequency	f_{sw}	5	kHz
Natural frequency of power measurement LPF	f_f	0.2	kHz
Bandwidth of the proposed power controller	ω_c	20	rad/s
Gain of proposed power controller	α	10	-

in green color). It becomes marginally stable in the weak grid when SCR = 2, and unstable when the SCR is further reduced to 1.2. In contrast, as shown in Fig. 4(d), the ePSGFLI is stable in the q-axis for all tested grid conditions. Hence, the ePSGFLI is expected to demonstrate stability and resilience across various grid connections.

IV. SIMULATION RESULTS

The performance of the proposed ePSGFLI is validated through the simulation of the system shown in Fig. 1 using MATLAB/Simulink and PLECS Blockset Packages. The system parameters employed in the simulation study are listed in Table 1. The simulation study investigates the effectiveness of the ePSGFLI strategy in response to active and reactive reference command changes and frequency deviations in both weak and strong grid connections. The applied step change tests provide significant insights into the dynamic response of the proposed controller, including its capacity to regulate output power, system stability, response speed, percentage of overshoot, and valuable information on adaptive controller tuning of the outer power controller. The effects of uncertainties in grid impedance parameters, grid voltage background harmonics, and PCC voltage feedforward are also investigated. Moreover, a comparative evaluation of the ePSGFLI is conducted against various control strategies, including GFLI, VMDPC, PSGFLI, LPV-PSGFLI, and GFMI.

A. PROPOSED ePSGFLI IN STRONG AND WEAK GRIDS

Fig. 5 shows the simulation results of the proposed control strategy in both strong and weak grid scenarios. The inverter operates in a steady-state condition initially, injecting 2 MW and 0 MVar in both scenarios. At $t = 0.2$ s, the active power reference command is increased to 4 MW to assess the inverter stability while injecting its full active power. Subsequently, the reactive power reference command is increased to 1.5 MVar at $t = 0.4$ s. Finally, a severe decrease of 5 Hz in the grid frequency is applied at $t = 0.6$ s to examine the system performance under frequency deviations.

Fig. 5(a), (c), (e), (g), and (i) presents the simulation results in the strong grid, while Fig. 5(b), (d), (f), (h), and (j) shows their dual in the weak grid. The three-phase output currents in the strong and weak grids are depicted in Fig. 5(a) and (b), respectively. Staring at $t = 0.58$ s and measured for one fundamental period, the total harmonic distortion (THD) values of these injected currents in both strong and weak grids are 1.85% and 1.15%, respectively. These values indicate that the proposed method complies with the IEEE 519 standard requirement of THD $\leq 5\%$ in low voltage networks [33].

The dq-components of the currents are shown in Fig. 5(c) and (d). It can be seen that the q-component of the inverter current in both grid conditions is regulated to zero while its d-component changes to track the desired active and reactive power set-points with zero steady-state errors. Fig. 5(e) and (f) shows the dq-components of the terminal voltage. In contrast to the GFLI scheme in which the q-component of the voltage is fixed at zero by the PLL, the proposed ePSGFLI varies the q-component to track the power set-points. Comparing the strong and weak grid operations, it is evident from Fig. 5(e) and (f) that the variations in the d-component of the terminal voltage are considerably higher in the weak grid.

The active and reactive power waveforms of the inverter in the strong and weak grid conditions are depicted in Fig. 5(g) and (h), respectively. The proposed controller tracks changes in the power set-points with zero steady-state errors, while demonstrating its capability to decouple the active and reactive power loops, as evidenced by the negligible impact of changes in active power on reactive power and vice versa. Finally, Fig. 5(i) and (j) demonstrates the effectiveness of the ePSGFLI in accurately tracking the significant 5 Hz change in grid frequency applied at $t = 6$ s. The results confirm the stability and robustness of the controller in regulating the inverter output, regardless of the grid condition.

Fig. 6 showcases the real-time adaptive tuning capability of the power controller proposed in (23). The simulation results presented in the figure demonstrate the ability of the ePSGFLI to adjust its controller parameters dynamically when operating the inverter in the weak grid with SCR = 2. This adaptive tuning capability ensures maintaining the desired bandwidth for the controller, leading to optimal dynamic performance of the inverter.

B. PROPOSED ePSGFLI IN LOW POWER INJECTION

Although the proposed ePSGFLI has several advantages, it can become unstable when the inverter operates at low levels of active power injection. To overcome this limitation, two approaches are suggested: injecting a certain amount of reactive power or freezing the parameters of the power controller for low values of the active power set-point. In this subsection, the latter solution is used. Fig. 7 shows the simulation results of the proposed controller in the strong grid with SCR = 10, with changes in the active power set-point while the reactive power is set to zero. For instance, the active power set-point is decreased from 4 to 0 MW at $t = 0.3$ s. As shown in the figure, the ePSGFLI tracks the desired power references accurately.

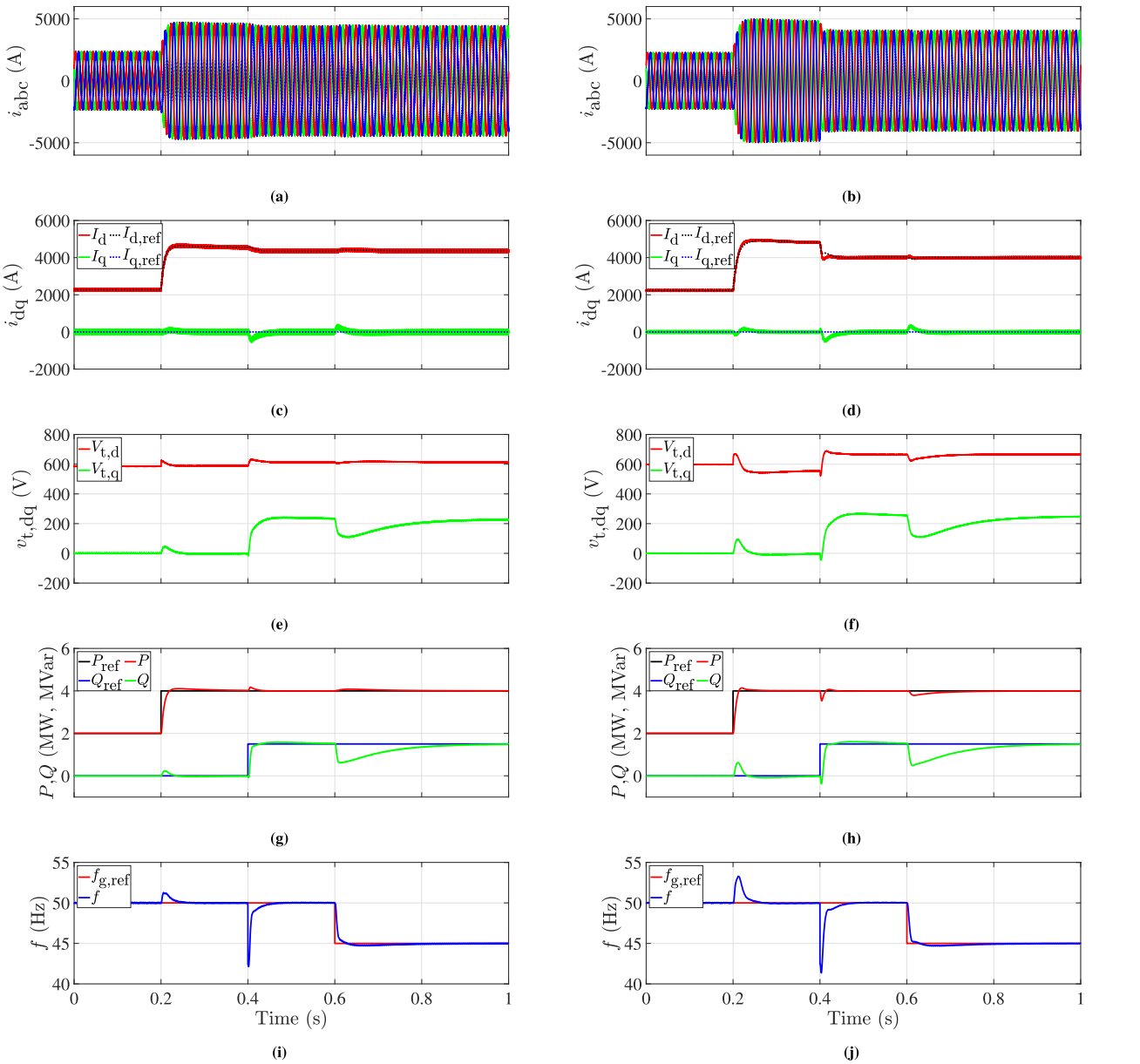

FIGURE 5. Simulation results of the proposed ePSGFLI operating in the strong grid (a),(c),(e),(g), and (i) with SCR = 10 and in the weak grid (b),(d),(f),(h), and (j) with SCR = 2 under variations in the active and reactive power set-points and frequency deviations. (a) and (b) Three-phase output current. (c) and (d) *dq*-components of the output current. (e) and (f) *dq*-components of the terminal voltage. (g) and (h) Output active and reactive power. (g) and (h) Estimated frequency generated by the ePSGFLI and its grid reference.

C. EFFECTS OF UNCERTAINTIES IN THE GRID IMPEDANCE PARAMETERS

To optimally tune the proposed controller, it is necessary to know the grid resistance and inductance (R_g, L_g) to calculate a_1 and a_2 presented in (14) and (15), respectively. While there are several online approaches for impedance estimation in the literature, errors may still occur in the estimation process [34]. Hence, this section presents a robustness analysis of the proposed ePSGFLI against errors in the grid impedance estimation.

Fig. 8 displays the simulation results of the ePSGFLI with uncertainties in the grid impedance estimation. Three case studies are analyzed here. The first case, referred to as $@Z_g$, assumes that the exact values of R_g and L_g are known in which SCR = 2. In the second case, referred to as $@0.8Z_g$, R_g, and L_g estimation errors of -20% are assumed. Finally, in the third case, referred to as $@1.2Z_g$, R_g and L_g estimation errors of $+20\%$ are assumed. It is worth mentioning that the selected error range $[-20\% \; -+20\%]$ for R_g and L_g estimation errors is higher than the expected errors, as reported in previous studies [34], [35]. Nonetheless, this deliberate choice of a wider error range is made to evaluate the performance of the proposed controller in a worst-case scenario. As shown in Fig. 8, despite small differences during the transients, it is evident

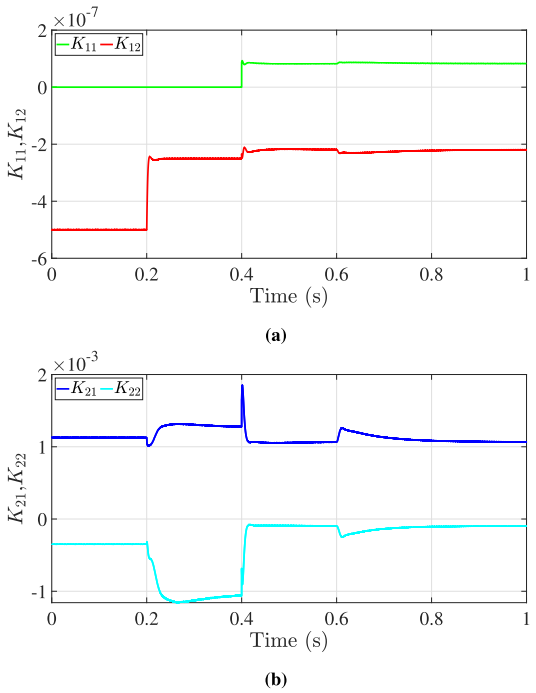

FIGURE 6. Adaptive tuning of the proposed power controller upon changes in the power references and 5 Hz frequency deviations in the weak grid with SCR = 2. (a) Control parameters of the active power channel. (b) Control parameters of the reactive power channel.

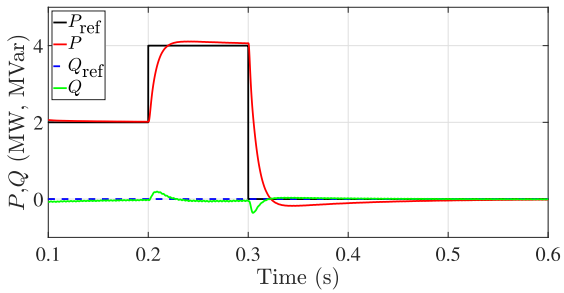

FIGURE 7. Simulation results of the proposed ePSGFLI upon changes in the active power set-point without reactive power support.

that the proposed controller is robust against uncertainties in the grid impedance parameters.

D. EFFECTS OF GRID VOLTAGE BACKGROUND HARMONICS

Unlike other tests, this section examines the performance of the ePSGFLI in a nonideal grid voltage source in order to consider power quality issues. Five different harmonics are considered to be presented in the grid voltage source. These harmonics are 3rd, 5th, 7th, 9th, and 11th, all with an amplitude of 3% of the fundamental voltage.

Fig. 9 presents the simulation results of the proposed ePSGFLI considering the nonideal grid voltage source. The test is conducted when the inverter is connected to the weak grid with SCR = 2 upon changes in the active and reactive power set-point at $t = 0.2$ and 0.4 s, respectively, and upon the 5 Hz frequency deviations in the grid frequency at $t = 0.6$ s.

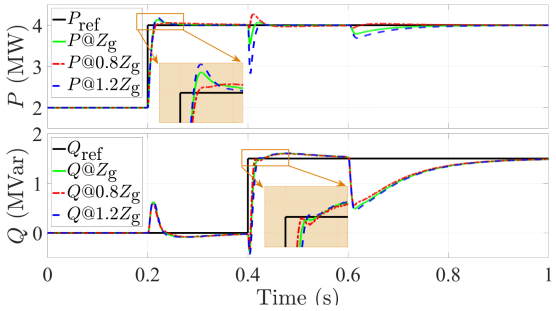

FIGURE 8. Simulation results evaluating the robustness of the proposed controller against uncertainties in the grid impedance.

Fig. 9(a) presents the simulated nonideal grid voltage source polluted with the 3rd, 5th, 7th, 9th, and 11th harmonics. It can be seen that the voltage waveform is no longer sinusoidal. Fig. 9(b) shows the frequency harmonic spectrum of the nonideal grid voltage source, with each added harmonic having an amplitude of 16.9 V or 3% V_g.

Fig. 9(c) and (d) presents the injected current to the grid and the output active and reactive power under the concerned harmonics. Compared with the results in the ideal grid voltage source shown in Fig. 5(b), (d), (f), (h), and (j), it can be seen that the proposed controller successfully tracks the desired active and reactive power set-points. However, there are more ripples due to the presence of the harmonics background. Fig. 9(e) demonstrates that the proposed controller accurately extracts the grid voltage frequency under the harmonic distortions before and after applying the frequency deviations at 0.6 s. Overall, this test shows that the proposed controller operates stably and injects the desired power references while considering power quality issues.

E. EFFECTS OF THE PCC VOLTAGE FEEDFORWARD

In conventional vector current control loops, feedforward terms are used to eliminate V_d and V_q terms in the equations based on the system model. These feedforward terms are employed to improve damping [36]. However, for ePSGFLI, the use of terminal voltage in the system equation removes the need for feedforward terms. Therefore, including feedforward terms for this specific control structure would actually disrupt the signals, resulting in degraded system performance. This section investigates the effects of PCC voltage feedforward on the performance of the proposed ePSGFLI through two case studies, as shown in Fig. 10.

The first case study, labeled $V_{ff} = 0$, studies the inverter performance without voltage feedforward, while the second case study, labeled $V_{ff} \neq 0$, considers the use of PCC voltage feedforward, in which a PLL is used to extract the frequency angle of the PCC voltage for conversion of the $v_{pcc,abc}$ components to the dq reference frame (V_d and V_q). Fig. 10 shows that the proposed control strategy performs well without PCC voltage feedforward. Power tracking is smooth and without significant overshoot. In contrast, the inverter dynamic performance deteriorates in the second case, with oscillations during

transients, and increased control rising time, particularly in reactive power. Another drawback of using PCC voltage feedforward is that using the PLL to extract the *dq* component of the PCC voltage contradicts the goal of the proposed method of eliminating the need for a PLL to enable seamless performance in both weak and strong grids.

F. COMPARISON OF ePSGFLI WITH GFLI

Fig. 11 displays simulation results of the GFLI and the proposed ePSGFLI in the weak grid with SCR = 2 under various test conditions, including changes in the active and reactive power set-points, grid frequency deviations, and a grid voltage sag at 0.2, 0.4, 0.6, and 1 s, respectively. The simulation results reveal poor dynamic performance of the GFLI during transients, where there are oscillations in the output power with each change in the power set-points. The GFLI is marginally stable, and this finding is demonstrated in the impedance analysis in Fig. 4(d). Additionally, the GFLI becomes unstable after applying of the grid voltage sag with a magnitude of 20%V_g. This unstable operation is caused by the reduction in the grid capacity, resulting in SCR < 2. In contrast, the ePSGFLI proves to be stable under all test conditions and regulates the output power to the desired set-points. During the steady state and for one fundamental period starting at $t = 0.58$ s, the THD value of the injected current by the conventional GFLI is identical to that of the proposed ePSGFLI control strategy, both achieving a THD value of 1.15%.

G. COMPARISON OF ePSGFLI WITH PSGFLI

This section provides a comparison between the performance of the proposed ePSGFLI and the conventional PSGFLI reported in [31]. Both inverter systems are examined under the same test conditions, which include changes in the active and reactive power set-points and frequency deviation by 5 Hz at 0.6 s in the weak grid with an SCR = 2.

Fig. 12 presents the simulation results of both control strategies. On the one hand, both controllers demonstrate the ability to track the desired power set-points and operate stably after the frequency deviation with zero steady-state error. On the other hand, it is evident that the transient response of the ePSGFLI is far better than that of the conventional PSGFLI. For example, the results show that the settling time and rise time of the active power are reduced compared to those of the conventional PSGFLI. Furthermore, the ePSGFLI reaches the steady-state condition with a fast dynamic response upon the frequency deviations at 0.6 s. As stated earlier, unlike the ePSGFLI, the control bandwidth of the conventional PSGFLI is a function of the operating point.

H. COMPARISON OF ePSGFLI WITH VMDPC AND LPV-PSGFLI

Fig. 13 compares the performance of the proposed ePSGFLI with the VMDPC and LPV-PSGFLI, in both strong and weak grids for the same test scenarios. The simulation starts with the inverter operating at a steady-state condition and injecting

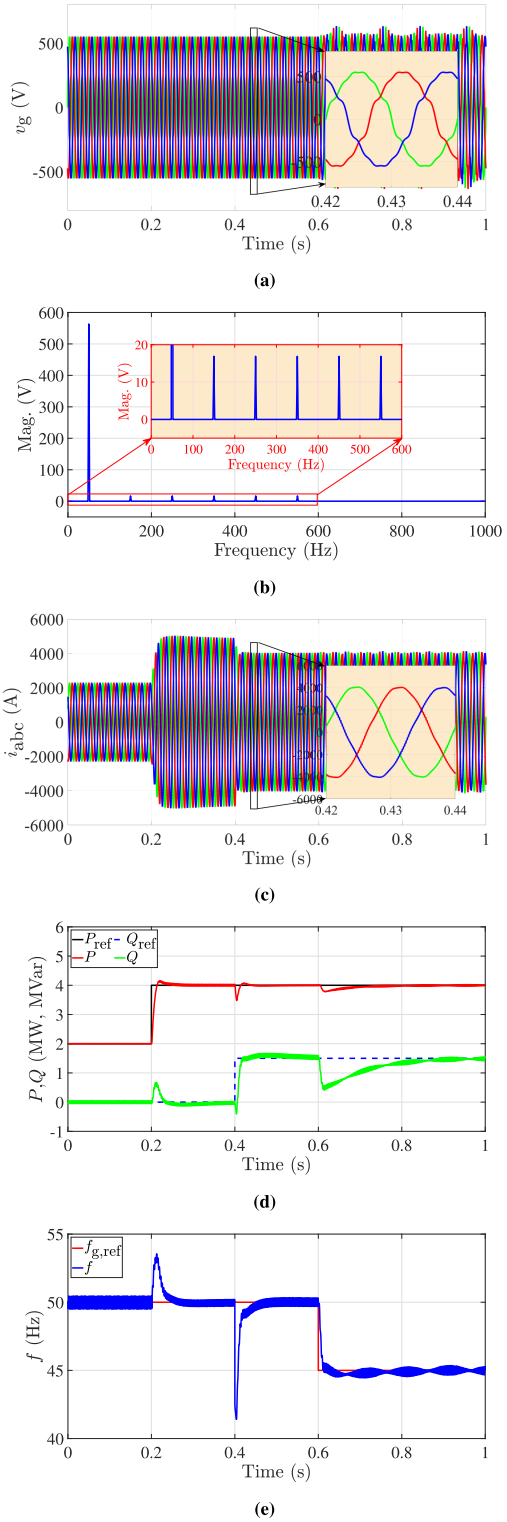

FIGURE 9. Simulation results of the proposed ePSGFLI in the weak grid with SCR = 2 when connected to nonideal grid voltage source polluted with five harmonics (3rd, 5th, 7th, 9th, and 11th, all with amplitude of 3%V_g). (a) Three-phase nonideal grid voltage source, (b) frequency harmonic spectrum of the grid voltage, (c) three-phase inverter output current, (d) output active and reactive power and their references, and (g) estimated frequency generated by the ePSGFLI and its grid reference.

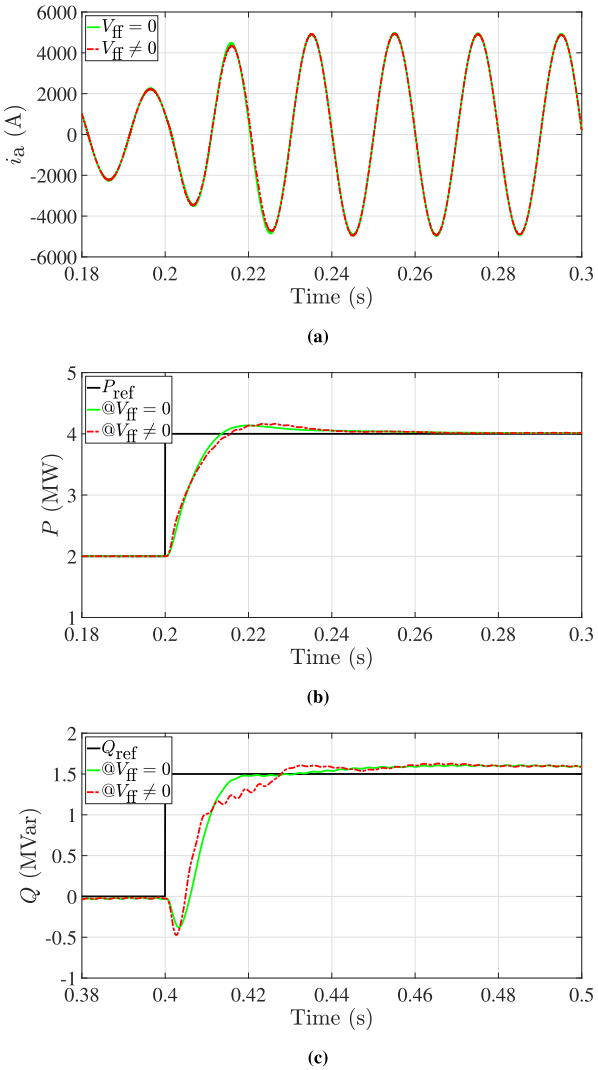

FIGURE 10. Simulation results of the proposed ePSGFLI in the weak grid with SCR = 2 considering the PCC voltage feedforward terms. (a) Output current of phase A, (b) output active power and its reference, and (c) output reactive power and its reference.

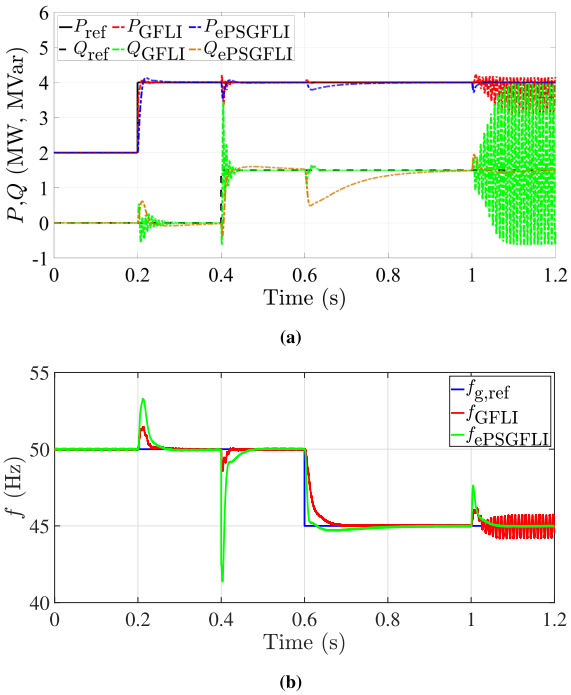

FIGURE 11. Simulation results comparing the conventional GFLI with the proposed ePSGFLI upon changes in the references power, 5 Hz frequency deviations, and 20% voltage sag in the grid voltage source. (a) Output power waveforms. (b) Frequency.

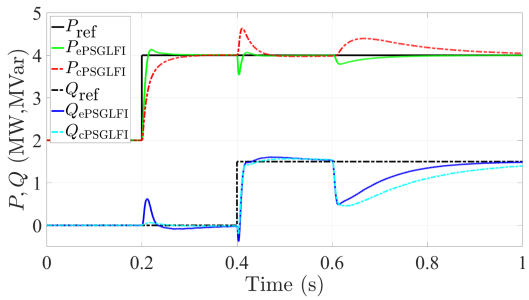

FIGURE 12. Simulation results show the comparison between the proposed ePSGFLI and the conventional PSGFLI in the weak grid upon changes in the active and reactive power set-points and frequency deviation by 5 Hz at 0.6 s.

2 MW of active power. At 2 s, the active power set-point is increased to 4 MW, and at 4 s, a step change in the grid frequency is introduced. In the strong grid, shown in Fig. 13(a), the ePSGFLI and LPV-PSGFLI exhibit faster dynamic performance than VMDPC after the changes in the power set-points. However, following the deviation of 5 Hz in the grid frequency, the reactive power of the LPV-PSGFLI experiences a significant decrease to approximately -1.6MVAR, while the active power exhibits a slight increase.

In the weak grid scenario, Fig. 13(b) and (c) illustrates the simulation results for two distinct frequency deviations, namely, 1 and 5 Hz, respectively. Despite slow response of the VMDPC and steady-state errors of the LPV-PSGFLI, all three controllers maintain stability following the 1 Hz frequency deviation. However, only the ePSGFLI demonstrates stable operation after the 5 Hz frequency deviation, accurately tracking power references with zero steady-state errors, as depicted in Fig. 13(c). It is noteworthy that the power waveforms are measured at the terminal for the LPV-PSGFLI and ePSGFLI, while at the PCC for the VMDPC.

I. COMPARISON OF ePSGFLI WITH GFMI

This section provides results for the conventional GFMI based on the virtual synchronous generator (VSG). The inverter system is examined in the same test conditions, upon changes in the active and reactive power set-points and frequency deviation by 0.1 Hz at 30 s in the weak grid with an SCR = 2. Fig. 14 illustrates how the VSG can effectively follow the desired power set-points and remain stable before the frequency deviation. Nonetheless, it should be emphasized that two important points can be distinguished when comparing the transient response of the proposed controller in Fig. 5

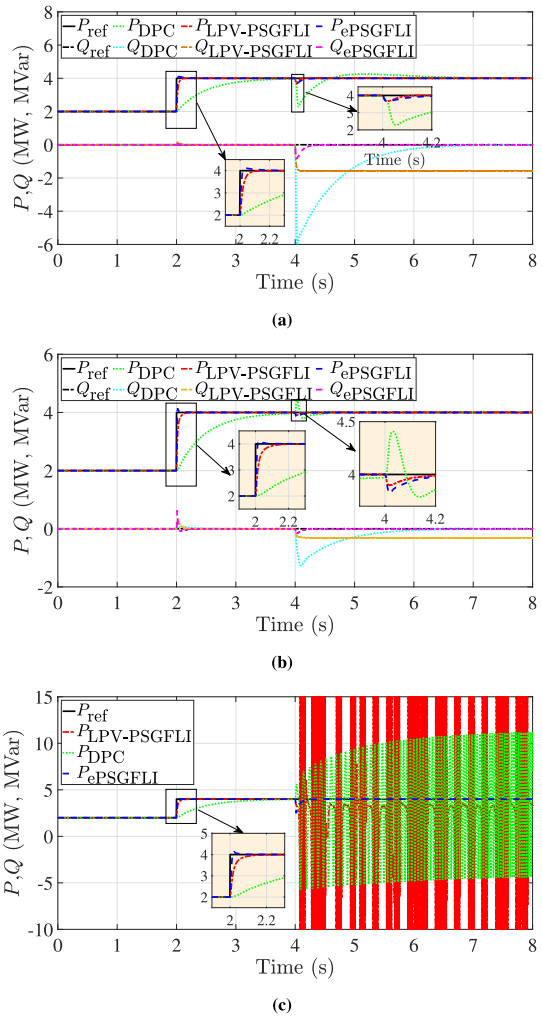

FIGURE 13. Simulation results of active and reactive power and their references of the VMDPC, LPV-PSGFLI and the proposed ePSGFLI upon changes in the power reference commands, and deviations in the grid frequency. (a) Strong grid with SCR = 10 and 5 Hz frequency deviation, (b) weak grid with SCR = 2 and 1 Hz frequency deviation, and (c) weak grid with SCR = 2 and 5 Hz frequency deviation.

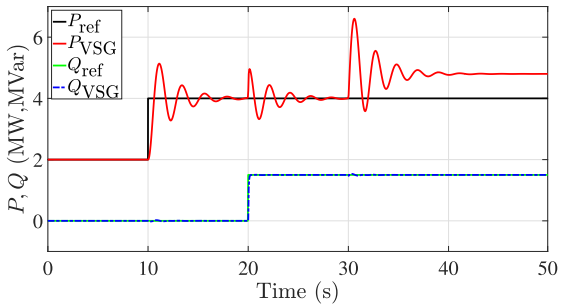

FIGURE 14. Simulation results show the performance of the conventional VSG in the weak grid upon changes in the active and reactive power set-points and frequency deviation by 0.1 Hz at 30 s.

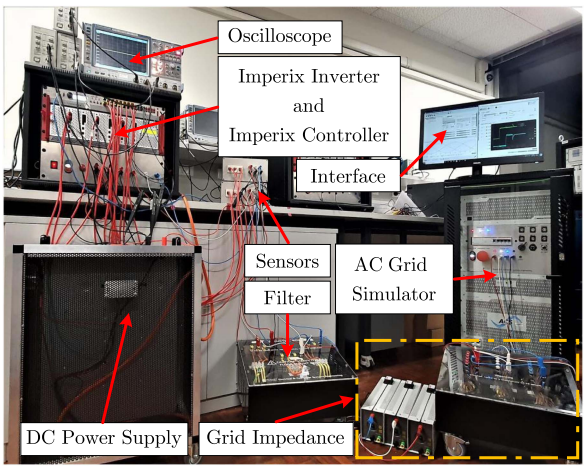

FIGURE 15. Experimental test-bed.

TABLE 2. Parameters Used for the Experimental Test-Bed

Parameter	Symbol	Value	Unit
Grid voltage (RMS, L-L)	v_g	100	V
Grid nominal frequency	f_g	50	Hz
Strong grid with SCR = 7.2	R_g, L_g	0.25, 3	Ω, mH
Weak grid with SCR = 1.38	R_g, L_g	1, 16	Ω, mH
Inverter rated active power	P_n	1	kW
Inverter rated reactive power	Q_n	1	kVar
DC bus voltage	v_{dc}	320	V
Filter inductance	L_f	4	mH
Filter resistance	R_f	0.1	Ω
Inverter PWM carrier frequency	f_{sw}	20	kHz
Natural frequency of power measurement LPF	f_f	0.2	kHz
Bandwidth of the proposed Power controller	ω_c	12.7	rad/s
Gain of proposed power controller	α	5	-

with that of the VSG. First, Fig. 14 indicates that the VSG active power settling time is significantly prolonged at approximately 10 s, and the overshoot upon changing the active power reference is excessively high at approximately 20%. Second, in the event of the frequency deviation occurring at 30 s, the VSG automatically adjusts its output active power to support the grid frequency. However, this adjustment results in a steady-state error in the output active power from the desired references as long as the grid frequency deviates from its nominal value of 50 Hz.

V. EXPERIMENTAL RESULTS

In this section, the proposed control strategy presented in Fig. 1 is validated through experimental results. The system parameters for the experiment are listed in Table 2. Fig. 15 shows a photograph of the experimental test-bed. It consists of a SiC-based two-level three-phase Imperix inverter supplied by a dc voltage source, an L filter, a series RL impedance representing the grid impedance, and a grid simulator. The inverter is controlled by a B-Box, which is a rapid control prototyping system for power electronic applications programmed directly via MATLAB/Simulink. The experimental data are collected through the B-Box and then exported as a CSV file for further analysis, visualization, and plotting.

It is worth noting that while the simulation parameters correspond to the simulation of a large-scale system to study

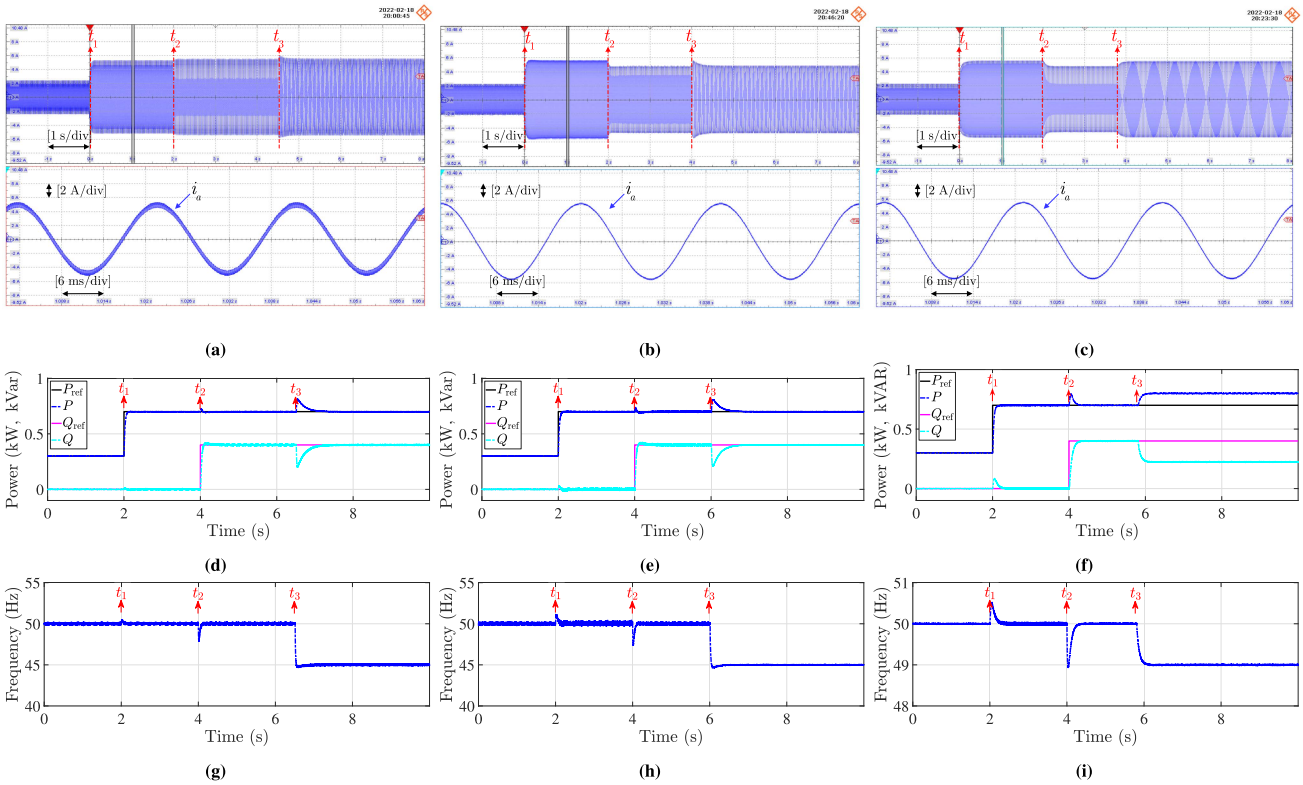

FIGURE 16. Experimental results show the PCC current waveform of phase A, the output power waveforms and the estimated frequency by the controller of the proposed ePSGFLI and the LPV-PSGFLI upon changes in the power reference set-points and in the grid frequency. (a), (d), and (g) Proposed ePSGFLI in a strong grid with SCR = 7.2. (b), (e), and (h) Proposed ePSGFLI in a weak grid with SCR = 1.38. (c), (f), and (i) LPV-PSGFLI in a weak grid with SCR = 1.38.

the stability of renewable energy integration at a real-world level, the experimental parameters correspond to a scaled-down version of the system due to the laboratory limitations. Furthermore, the values of the impedance of the grid located between the inverter output filter and the grid simulator are utilized in the adaptive tuning of the controller using the values listed in Table 1. In practical connections, the grid impedance is time-varying and can be estimated in real-time using an online technique [34], [35], [37], [38].

The experimental evaluation of the proposed ePSGFLI strategy in both strong and weak grids is conducted through two tests. An additional test is conducted to verify the shortcoming of the LPV-PSGFLI method during grid frequency deviations. In each test, step changes in the active and reactive power set-points and the grid frequency are applied. The time instances when these three changes are applied are referred to as t_1, t_2, and t_3, respectively, as shown in Fig. 16. Initially, the inverter operates in a steady state with power set-points of $P_{\text{ref}} = 300$ W and $Q_{\text{ref}} = 0$ Var. At time instances t_1 and t_2, the active and reactive power set-points are respectively modified to $P_{\text{ref}} = 700$ W and $Q_{\text{ref}} = 400$ Var. Subsequently, a step change in the grid frequency is introduced at time instance t_3. In the first and second tests, a 5 Hz step change is applied to assess the robustness of the ePSGFLI to frequency deviations in the strong and weak grids, respectively. However, the third test employs only a 1 Hz step change to verify the steady-state errors of the LPV-PSGFLI.

A. TEST 1:PROPOSED ePSGFLI IN A STRONG GRID

Fig. 16(a), (d), and (g) depicts the experimental results when the proposed controller is connected to the strong grid with SCR = 7.2. The figures show the inverter output current, power tracking capability, and estimated frequency of the proposed ePSGFLI, respectively. It is evident that the ePSGFLI ensures seamless dynamic performance and achieves a smooth transition without any significant oscillations upon changes of the active and reactive power set-points at t_1 and t_2, respectively. The ePSGFLI accurately regulates the output active and reactive power to their desired set-points with zero steady-state errors. Moreover, the ePSGFLI accurately tracks the grid frequency upon the grid frequency deviation from 50 to 45 Hz at t_3, as depicted in Fig. 16(g).

B. TEST 2: PROPOSED ePSGFLI IN A WEAK GRID

Fig. 16(b), (e), and 16(h) presents the experimental results of the proposed ePSGFLI in the weak grid with SCR = 1.38. It can be observed that the ePSGFLI strategy is robust and ensures seamless transients. Upon the frequency deviation to 45 Hz at t_3, the proposed controller is still capable of

TABLE 3. COMPARISON SUMMARY of the PROPOSED PLL-LESS ePSGFLI WITH OTHER PLL-BASED and PLL-LESS CONTROL STRATEGIES

Criteria	GFLI	GFMI	DPC	PSGFLI	LPV-PSGFLI	Proposed ePSGFLI
Performance in strong grid	✓	✗	✗	✓	✓	✓
Performance in weak grid	✗	✓	✓	✓	✓	✓
Preserving the controller bandwidth for different operating points	✗	✗	✗	✗	✓	✓
Adaptive control tuning	✗	✗	✗	✗	✓	✓
Does not require a PLL	✗	✓	✓	✓	✓	✓
Stability under frequency deviations	✓	✓	✗	✓	✗	✓

The performance of the controller is divided into: ✓ very well (stable), ✗ poor (or unstable).

regulating the output active and reactive power to their desired references. Compare to Test 1, it is evident that the proposed controller maintain almost identical dynamic performance in Test 2 during the transient periods at t_1, t_2, and t_3. This consistent response is achieved irrespective of the grid strength (strong or weak grids) due to the incorporation of grid impedance information in the adaptive tuning of the output power control loop. As a result, this approach effectively decouples the control response from the grid strength, enabling the system to maintain a unified response regardless of changes in grid conditions.

C. TEST 3: LPV-PSGFLI IN A WEAK GRID

This test assesses the performance of the LPV-PSGFLI when connected to the same weak grid. Fig. 16(c), (f), and (i) present the experimental results of the inverter output current, power, and frequency estimated by the LPV-PSGFLI, respectively. In contrast to the performance of the proposed controller demonstrated in Test 2, the LPV-PSGFLI exhibits poor dynamic performance when the grid frequency deviates from its nominal value of 50 Hz. The reduction in the grid frequency to 49 Hz at t_3 leads to steady-state errors in the inverter output power. These experimental findings align with the simulation results presented earlier in Fig. 13(a) and (c). Lastly, it is noteworthy that Fig. 16(a) reveals high-frequency ripples in i_a, which result from the high SCR value (small Z_g) employed to simulate a strong grid. However, as depicted in Fig. 16(b) and (c), the high-frequency ripples in i_a are reduced by decreasing the SCR value (large Z_g).

Lastly, it is worth noting that Fig. 16(a) reveals the presence of high-frequency ripples in i_a, which stem from the high SCR value (corresponding to a small Z_g) employed to simulate a strong grid. However, as depicted in Fig. 16(b) and (c), the high-frequency ripples in i_a are reduced due to the utilization of a small SCR value (corresponding to a larger Z_g), where Z_g acts as an additional current filter in series with the inverter output filter (L_f).

Table 3 provides a comparison between the proposed PLL-less ePSGFLI with other PLL-less (PSGFLI, LPV-PSGFLI, VMDPC) and conventional PLL-based GFLI control strategies. Furthermore, the proposed controller is also compared with the conventional GFMI. The evaluation highlights the strengths and weaknesses of each approach. In summary, the following key observations can be drawn.

1) The proposed control is capable of working in both strong and weak grids.
2) The proposed control strategy preserves the controller bandwidth for any given operating point.
3) Out of the PLL-less control strategies, only the proposed controller is stable under large frequency deviations.

VI. CONCLUSION

This article proposes an enhanced frequency control for power-synchronized PLL-less grid-following inverters, ensuring reliable and stable performance in diverse operating conditions, including strong and weak grid connections and frequency deviations. By internally generating the phase angle, the approach eliminates the need for a PLL, ensuring robustness even in ultraweak grids. The suggested strategy is capable of regulating inverter terminal power by measuring output current and utilizing voltage reference, eliminating the need for a voltage sensor. The adaptive tuning of the outer 2-by-2 power controller, combined with the selection of the desired open-loop transfer function matrix, ensures the desired dynamic performance and stable operation at any given operating point. It effectively decouples the active and reactive power loops and accurately tracks the grid frequency, even in the presence of significant frequency deviations. This proposed strategy outperforms other existing control strategies in all conditions, making it a promising solution for robust and stable control of PLL-less grid-following inverters across various grid strengths and abnormal frequency conditions.

REFERENCES

[1] A. S. Anees, "Grid integration of renewable energy sources: Challenges, issues and possible solutions," in *Proc. IEEE 5th India Int. Conf. Power Electron.*, 2012, pp. 1–6.
[2] M. Liserre, R. Cardenas, M. Molinas, and J. Rodriguez, "Overview of multi-mw wind turbines and wind parks," *IEEE Trans. Ind. Electron.*, vol. 58, no. 4, pp. 1081–1095, Apr. 2011.
[3] A. Luna et al., "Grid voltage synchronization for distributed generation systems under grid fault conditions," *IEEE Trans. Ind. Appl.*, vol. 51, no. 4, pp. 3414–3425, Jul./Aug. 2015.

[4] M. Lu, S. Dhople, and B. Johnson, "Benchmarking nonlinear oscillators for grid-forming inverter control," *IEEE Trans. Power Electron.*, vol. 37, no. 9, pp. 10250–10266, Sep. 2022.
[5] B. Bahrani, A. Rufer, S. Kenzelmann, and L. A. Lopes, "Vector control of single-phase voltage-source converters based on fictive-axis emulation," *IEEE Trans. Ind. Appl.*, vol. 47, no. 2, pp. 831–840, Mar./Apr. 2011.
[6] Y. Li, Y. Gu, and T. C. Green, "Revisiting grid-forming and grid-following inverters: A duality theory," *IEEE Trans. Power Syst.*, vol. 37, no. 6, pp. 4541–4554, Nov. 2022.
[7] X. Wang, M. G. Taul, H. Wu, Y. Liao, F. Blaabjerg, and L. Harnefors, "Grid-synchronization stability of converter-based resources–An overview," *IEEE Open J. Ind. Appl.*, vol. 1, no. 8, pp. 115–134, Aug. 2020.
[8] F. Blaabjerg, R. Teodorescu, M. Liserre, and A. V. Timbus, "Overview of control and grid synchronization for distributed power generation systems," *IEEE Trans. Ind. Electron.*, vol. 53, no. 5, pp. 1398–1409, Oct. 2006.
[9] D. B. Rathnayake et al., "Grid forming inverter modeling, control, and applications," *IEEE Access*, vol. 9, pp. 114781–114807, 2021.
[10] C. Henderson, A. Egea-Alvarez, T. Kneuppel, G. Yang, and L. Xu, "Grid strength impedance metric: An alternative to SCR for evaluating system strength in converter dominated systems," *IEEE Trans. Power Del.*, to be published, doi: 10.1109/TPWRD.2022.3233455.
[11] W. Zhou, Y. Wang, R. E. Torres-Olguin, and Z. Chen, "Effect of reactive power characteristic of offshore wind power plant on low-frequency stability," *IEEE Trans. Energy Convers.*, vol. 35, no. 2, pp. 837–853, Jun. 2020.
[12] W. Zhou, N. Mohammed, and B. Bahrani, "Comprehensive modeling, analysis, and comparison of state-space and admittance models of PLL-based grid-following inverters considering different outer control modes," *IEEE Access*, vol. 10, pp. 30109–30146, 2022.
[13] Z. Zhou, W. Wang, D. Ramasubramanian, E. Farantatos, and G. M. Huang, "Small signal stability of phase locked loop based current-controlled inverter in 100% inverter-based system," *IEEE Trans. Sustain. Energy*, to be published, doi: 10.1109/TSTE.2023.3241094.
[14] S. Golestan, E. Ebrahimzadeh, B. Wen, J. M. Guerrero, and J. C. Vasquez, "dq-frame impedance modeling of three-phase grid-tied voltage source converters equipped with advanced PLLs," *IEEE Trans. Power Electron.*, vol. 36, no. 3, pp. 3524–3539, Mar. 2021.
[15] J. Z. Zhou, H. Ding, S. Fan, Y. Zhang, and A. M. Gole, "Impact of short-circuit ratio and phase-locked-loop parameters on the small-signal behavior of a VSC-HVDC converter," *IEEE Trans. Power Del.*, vol. 29, no. 5, pp. 2287–2296, Oct. 2014.
[16] B. Wen, D. Boroyevich, R. Burgos, P. Mattavelli, and Z. Shen, "Analysis of DQ small-signal impedance of grid-tied inverters," *IEEE Trans. Power Electron.*, vol. 31, no. 1, pp. 675–687, Jan. 2016.
[17] H. Nian, B. Hu, C. Wu, L. Chen, Y. Xu, and F. Blaabjerg, "Analysis and reshaping on impedance characteristic of DFIG system based on symmetrical PLL," *IEEE Trans. Power Electron.*, vol. 35, no. 11, pp. 11720–11730, Nov. 2020.
[18] L. Huang, C. Wu, D. Zhou, and F. Blaabjerg, "A double-PLLS-based impedance reshaping method for extending the stability range of grid-following inverter under weak grid," *IEEE Trans. Power Electron.*, vol. 37, no. 4, pp. 4091–4104, Apr. 2022.
[19] M. F. M. Arani and Y. A.-R. I. Mohamed, "Analysis and performance enhancement of vector-controlled VSC in HVDC links connected to very weak grids," *IEEE Trans. Power Syst.*, vol. 32, no. 1, pp. 684–693, Jan. 2017.
[20] M. Z. Mansour, M. H. Ravanji, A. Karimi, and B. Bahrani, "Small-signal synchronization stability enhancement of grid-following inverters via a feedback linearization controller," *IEEE Trans. Power Del.*, vol. 37, no. 5, pp. 4335–4344, Oct. 2022.
[21] T. Noguchi, H. Tomiki, S. Kondo, and I. Takahashi, "Direct power control of PWM converter without power-source voltage sensors," *IEEE Trans. Ind. Appl.*, vol. 34, no. 3, pp. 473–479, May/Jun. 1998.
[22] M. Malinowski, M. Jasinski, and M. P. Kazmierkowski, "Simple direct power control of three-phase PWM rectifier using space-vector modulation (DPC-SVM)," *IEEE Trans. Ind. Electron.*, vol. 51, no. 2, pp. 447–454, Apr. 2004.
[23] S. Vazquez, A. Marquez, R. Aguilera, D. Quevedo, J. I. Leon, and L. G. Franquelo, "Predictive optimal switching sequence direct power control for grid-connected power converters," *IEEE Trans. Ind. Electron.*, vol. 62, no. 4, pp. 2010–2020, Apr. 2015.
[24] D.-K. Choi and K.-B. Lee, "Dynamic performance improvement of AC/DC converter using model predictive direct power control with finite control set," *IEEE Trans. Ind. Electron.*, vol. 62, no. 2, pp. 757–767, Feb. 2015.
[25] Y. Gui, C. Kim, C. C. Chung, J. M. Guerrero, Y. Guan, and J. C. Vasquez, "Improved direct power control for grid-connected voltage source converters," *IEEE Trans. Ind. Electron.*, vol. 65, no. 10, pp. 8041–8051, Oct. 2018.
[26] M. Bollen, M. Olofsson, A. Larsson, S. Rönnberg, and M. Lundmark, "Standards for supraharmonics (2 to 150 khz)," *IEEE Electromagn. Compat. Mag.*, vol. 3, no. 1, pp. 114–119, 1st Quarter 2014.
[27] M. B. Marz, "Interharmonics: What they are, where they come from and what they do," in *Proc. Minnesota PowerSyst. Conf. Paper*, 2016, pp. 1–8.
[28] A. Sangwongwanich and F. Blaabjerg, "Mitigation of interharmonics in PV systems with maximum power point tracking modification," *IEEE Trans. power Electron.*, vol. 34, no. 9, pp. 8279–8282, Sep. 2019.
[29] Y. Gui, X. Wang, H. Wu, and F. Blaabjerg, "Voltage-modulated direct power control for a weak grid-connected voltage source inverters," *IEEE Trans. Power Electron.*, vol. 34, no. 11, pp. 11383–11395, Nov. 2019.
[30] S. M. Hoseinizadeh, S. Ouni, H. Karimi, M. Karimi-Ghartemani, and K. L. Lian, "Comparison of PLL-based and PLL-less vector current controllers," *IEEE Trans. Emerg. Sel. Topics Power Electron.*, vol. 10, no. 1, pp. 436–445, Feb. 2022.
[31] B. Bahrani, "Power-synchronized grid-following inverter without a phase-locked loop," *IEEE Access*, vol. 9, pp. 112163–112176, 2021.
[32] M. Z. Mansour, M. H. Ravanji, A. Karimi, and B. Bahrani, "Linear parameter-varying control of a power-synchronized grid-following inverter," *IEEE Trans. Emerg. Sel. Topics Power Electron.*, vol. 10, no. 2, pp. 2547–2558, Apr. 2022.
[33] *IEEE Recommended Practice and Requirements for Harmonic Control in Electric Power Systems*, IEEE Std 519-2014 (Revision of IEEE Std 519- 1992), IEEE Standards Association, New York, NY, USA, pp. 1–29, 2014.
[34] N. Mohammed, M. Ciobotaru, and G. Town, "Fundamental grid impedance estimation using grid-connected inverters: A comparison of two frequency-based estimation techniques," *IET Power Electron.*, vol. 13, no. 13, pp. 2730–2741, 2020.
[35] N. Mohammed, T. Kerekes, and M. Ciobotaru, "An online event-based grid impedance estimation technique using grid-connected inverters," *IEEE Trans. Power Electron.*, vol. 36, no. 5, pp. 6106–6117, May 2021.
[36] M. H. Ravanji, D. B. Rathnayake, M. Z. Mansour, and B. Bahrani, "Impact of voltage-loop feedforward terms on the stability of grid-forming inverters and remedial actions," *IEEE Trans. Energy Convers.*, to be published, doi: 10.1109/TEC.2023.3246566.
[37] N. Mohammed, M. Ciobotaru, and G. Town, "An improved grid impedance estimation technique under unbalanced voltage conditions," in *Proc. IEEE PES Innov. Smart Grid Technol. Europe*, 2019, pp. 1–5.
[38] N. Mohammed and M. Ciobotaru, "Fast and accurate grid impedance estimation approach for stability analysis of grid-connected inverters," *Electric Power Syst. Res.*, vol. 207, 2022, Art. no. 107831.

NABIL MOHAMMED (Member, IEEE) received the bachelor's degree (Hons.) in electrical power engineering from Tishreen University, Latakia, Syria, in 2013, the M.Eng. degree in electrical engineering from Universiti Teknologi Malaysia, Johor Bahru, Malaysia, in 2017, and the Ph.D. degree in power electronics from Macquarie University, Sydney, NSW, Australia, in 2022.

In 2019, he was a Visiting Researcher with the Department of Energy Technology, Aalborg University, Aalborg, Denmark. He is currently a Postdoctoral Research Fellow with Monash University, Clayton, VIC, Australia. His research interests include power electronic converters, grid integration of renewable energy resources, microgrids, energy storage and management systems, and modeling and control of electric power systems.

MOHAMMAD HASAN RAVANJI (Member, IEEE) received the B.Sc., M.Sc., and Ph.D. degrees in electrical power engineering from the Sharif University of Technology (SUT), Tehran, Iran, in 2012, 2014, and 2020, respectively.

He was a Visiting Student with the University of Waterloo, Waterloo, ON, Canada, from October 2017 to April 2018. Furthermore, he was with the Iran Grid Management Company (IGMC), Tehran, Iran, as a Researcher in their system planning and dynamic studies group from February 2019 to July 2020. From May 2021 to January 2023, he was a Postdoctoral Research Fellow with Monash University, Melbourne, Australia. Currently, he is an Assistant Professor with the Electrical Engineering Department, SUT, where he focuses on the design, control, analysis, dynamics, and operation of grid-following and grid-forming inverter-based renewable resources. His research interests include stability studies and dynamic model reduction of large-scale power systems.

WEIHUA ZHOU (Member, IEEE) was born in Anhui, China, in 1993. He received the B.Eng. degree in electrical engineering from the Honors College, Northwestern Polytechnical University, Xi'an, China, in 2014, the M.Sc. degree in electrical engineering from the School of Automation, Northwestern Polytechnical University, in 2017, and the Ph.D. degree in power electronics from the Department of Energy Technology, Aalborg University, Aalborg, Denmark, in 2020.

From November 2015 to May 2016, he was a Junior Research Assistant with the Department of Mechanical and Automation Engineering, The Chinese University of Hong Kong, Hong Kong. From August 2020 to November 2020, he was a Visiting Scholar with the Department of Marine Technology, Norwegian University of Science and Technology, Trondheim, Norway. In 2021, he was a Postdoctoral Fellow with the Department of Electrical Engineering, KU Leuven, Leuven, Belgium. He is currently a Postdoctoral Research Fellow with the Department of Electrical and Computer Systems Engineering, Monash University, Melbourne, Australia. His research interests include modeling and control of power electronic converters, energy storage systems, and stability analysis and enhancement of power electronic and underground cable-based modern power systems.

BEHROOZ BAHRANI (Senior Member, IEEE) received the B.Sc. degree from the Sharif University of Technology, Tehran, Iran, the M.Sc. degree from the University of Toronto, Toronto, ON, Canada, and the Ph.D. degree from the École Polytechnique Fédérale de Lausanne (EPFL), Lausanne, Switzerland, in 2006, 2008, and 2012, respectively, all in electrical engineering.

From September 2012 to September 2015, he was a Postdoctoral Fellow with several institutions including EPFL, Purdue University, West Lafayette, IN, USA, Georgia Institute of Technology, Atlanta, GA, USA, and the Technical University of Munich, Munich, Germany. Since 2015, he has been with Monash University, Clayton, Australia, where currently, he is a Senior Lecturer and the Director of the Grid Innovation Hub. His research interests include control of power electronics systems, applications of power electronics in power and traction systems, and grid integration of renewable energy resources.